



**HAL**  
open science

## Cs diffusion mechanisms in UO<sub>2</sub> investigated by SIMS, TEM, and atomistic simulations

C. Panetier, Y. Pison, C. Gaillard, D. Mangin, J. Amodeo, J. Morthomas, T. Wiss, A. Benedetti, R. Ducher, R. Dubourg, et al.

► **To cite this version:**

C. Panetier, Y. Pison, C. Gaillard, D. Mangin, J. Amodeo, et al.. Cs diffusion mechanisms in UO<sub>2</sub> investigated by SIMS, TEM, and atomistic simulations. *The Journal of Chemical Physics*, 2022, 156 (4), pp.044705. 10.1063/5.0076358 . hal-03867319

**HAL Id: hal-03867319**

**<https://hal.science/hal-03867319v1>**

Submitted on 23 Nov 2022

**HAL** is a multi-disciplinary open access archive for the deposit and dissemination of scientific research documents, whether they are published or not. The documents may come from teaching and research institutions in France or abroad, or from public or private research centers.

L'archive ouverte pluridisciplinaire **HAL**, est destinée au dépôt et à la diffusion de documents scientifiques de niveau recherche, publiés ou non, émanant des établissements d'enseignement et de recherche français ou étrangers, des laboratoires publics ou privés.

# Cs diffusion mechanisms in UO<sub>2</sub> investigated by SIMS, TEM and atomistic simulations

C. Panetier<sup>a</sup>, Y. Pison<sup>a,b\*</sup>, C. Gaillard<sup>a</sup>, D. Mangin<sup>c</sup>, J. Amodeo<sup>d,e</sup>, J. Morthomas<sup>d</sup>, T. Wiss<sup>f</sup>, A. Benedetti<sup>f</sup>,  
R. Ducher<sup>g</sup>, R. Dubourg<sup>g</sup>, N. Moncoffre<sup>a</sup>

<sup>a</sup> Univ Lyon, Univ Claude Bernard Lyon 1, CNRS/IN2P3, IP2I Lyon, UMR 5822, F-69622, Villeurbanne, France

<sup>b</sup> Univ Lyon, UCBL, IUT Lyon-1, Département chimie, F-69622, Lyon, France

<sup>c</sup> IJL, Université de Lorraine, CNRS : UMR7198 – CS 14234 54042 Nancy Cedex, France

<sup>d</sup> Univ Lyon, INSA Lyon, UCBL, CNRS, MATEIS, UMR5510, 69621 Villeurbanne, France

<sup>e</sup> Aix Marseille Univ., Université de Toulon, CNRS, IM2NP, Marseille, France

<sup>f</sup> European Commission, DG Joint Research Centre, Directorate G –Nuclear Safety and Security, PO box 2340, D-76125 Karlsruhe, Germany

<sup>g</sup> IRSN, LETR – BP3 13115 St-Paul-Lez-Durance Cedex, France

**\* Corresponding author:** Yves PIPON

E-mail: [y.pison@ipnl.in2p3.fr](mailto:y.pison@ipnl.in2p3.fr)

Postal address: Université de Lyon, UCBL, IP2I, Campus LyonTech La Doua, 4 rue Enrico Fermi, 69622 Villeurbanne cedex, France

## Highlights

New insights on Cs diffusion mechanisms in UO<sub>2</sub> derived from atomistic calculations obtained with semi-empirical potentials and supported by SIMS and TEM experimental data.

Keywords: UO<sub>2</sub>, Cs, diffusion, SIMS, MD, TEM

30 **ABSTRACT**

31 Experimental investigations and atomistic simulations are combined to study the cesium diffusion  
32 processes at high temperature in  $\text{UO}_2$ . After  $^{133}\text{Cs}$  implantation in  $\text{UO}_2$  samples, diffusion coefficients  
33 are determined using the depth profile evolution after annealing as measured by secondary ion mass  
34 spectrometry. An activation energy of  $1.8 \pm 0.2$  eV is subsequently deduced in the 1300-1600°C  
35 temperature range. Experimental results are compared to nudged elastic band simulations performed  
36 for different atomic paths including several types of uranium vacancy defects. Activation energies  
37 ranging from 0.49 up to 2.34 eV are derived, showing the influence of the defect (both in terms of type  
38 and concentration) on the Cs diffusion process. Finally, molecular dynamics simulations are performed,  
39 allowing the identification of preferential Cs trajectories that corroborate experimental observations.

40

41

42

## 43 1. INTRODUCTION

44 After major nuclear accidents (e.g., Chernobyl 1986, Fukushima Daichii 2011), large quantities of  $^{137}\text{Cs}$ ,  
45 a highly radiotoxic element with a half-life of 30 years, were disseminated outside the nuclear power  
46 plants with catastrophic consequences for the environment [1]. Hence, it is essential to improve our  
47 knowledge about the behaviour of this fission product (FP) present in nuclear fuels to better anticipate  
48 the implications of such events. To tackle this problem, several international research programs such  
49 as VERCORS, VEGA or VERDON [2–6] have focused on the FP behaviour in irradiated nuclear fuels  
50 (mainly  $\text{UO}_2$ ) in order to investigate several accidental scenarios (including atmosphere and  
51 temperature variations). As a main output, after an initial cesium release at  $1500^\circ\text{C}$ , a strong release  
52 was measured when the nuclear fuel was subjected to high temperatures (above  $2000\text{--}2300^\circ\text{C}$ ),  
53 confirming the volatile nature of cesium. Nevertheless, only few information about the underlying  
54 migration mechanisms are available due to the complexity of the parameters involved, which include  
55 variations in atmosphere composition, temperature, burnup and number of defects.

56 On the other hand, literature data show that Cs diffusion coefficients were exclusively determined  
57 from post-irradiation annealing release measurements using the Booth model [7] which is an indirect  
58 way to calculate apparent diffusion coefficients including among others the effect of extended defects  
59 and other fission product contributions. These diffusion coefficients were fitted using an Arrhenius  
60 law, giving access to activation energies ( $E_a$ ) and pre-exponential factors ( $D_0$ ) ranging from 1.6 eV to  
61 4.3 eV and from  $2.1 \cdot 10^{-8} \text{ cm}^2 \text{ s}^{-1}$  and  $3.4 \cdot 10^{-2} \text{ cm}^2 \text{ s}^{-1}$ , respectively, within the  $1450\text{--}2500^\circ\text{C}$  temperature  
62 range [5,8]. Such high discrepancies can be explained by the differences in irradiation history between  
63 all the experiments. Therefore, in order to get better insights on the diffusion mechanisms, the role of  
64 defects created during irradiation has to be assessed.

65 For this purpose, several authors performed atomistic simulations to provide inputs about Cs  
66 incorporation and mobility at various positions within the  $\text{UO}_2$  unit cell [9–12]. These studies show that  
67 cesium is favourably incorporated in uranium vacancies ( $V_U$ ), sole or in clusters of defects that contain  
68 oxygen vacancies ( $V_O$ ) such as the divacancy ( $V_U + V_O$ ), the Schottky defects ( $V_U + 2V_O$ ) or the  
69 tetravacancy ( $2V_U + 2V_O$ ). Furthermore, Gupta *et al.* determined Cs and U migration energy barriers  
70 between uranium vacancies in the  $\langle 110 \rangle$  direction using the nudged elastic band (NEB) method and  
71 obtained activation energies of 2.72 eV and 5.6 eV, respectively [9,13]. Hence, these studies  
72 emphasized that uranium diffusion is the rate limiting process that controls the Cs diffusion in  $\text{UO}_2$ .  
73 However, these NEB simulations represented a simplified first approach, ignoring complex pathways  
74 and other major defects such as Schottky defects. Therefore, the present study proposes new insights  
75 on the Cs thermal behaviour in  $\text{UO}_2$  coupling direct experimental observations and atomistic

76 calculations. It aims at determining Cs diffusion mechanisms and associated kinetics considering the  
77 major point defects (single vacancies, divacancies and Schottky defect) associated to the UO<sub>2</sub> lattice.  
78 For this purpose, ion implantation is used to introduce cesium in UO<sub>2</sub> pellets which are further  
79 annealed at temperatures representative of normal and accidental conditions in a light water reactor  
80 (LWR) fuel i.e., in the 1000°C to 1600°C temperature range. Cesium depth profiles are measured by  
81 secondary ion mass spectrometry (SIMS), both before and after annealing. Diffusion coefficients of  
82 cesium in UO<sub>2</sub> are then determined from the depth profile evolution in the 1300-1600°C temperature  
83 range. In parallel, atomistic calculations using empirical potentials are performed to identify the  
84 elementary diffusion processes. First, Cs migration energies in UO<sub>2</sub> are calculated for predetermined  
85 atomic trajectories associated to different defects in the crystal using the NEB method. Then,  
86 molecular dynamic (MD) outcomes allow to identify preferential elementary jump processes of Cs  
87 diffusion at high temperature.

88

## 89 **2. METHODS**

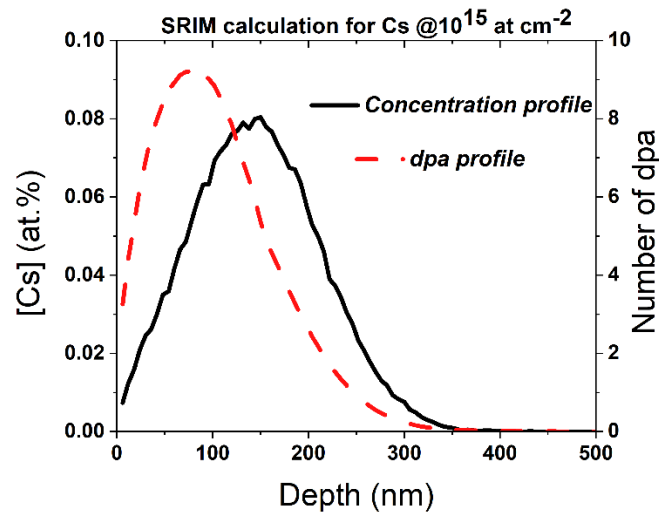
### 90 **2.1 Experimental procedure**

91 We used depleted UO<sub>2</sub> pellets (0.2 at.% of <sup>235</sup>U), provided by the Framatome company and sintered at  
92 1750°C under a reducing atmosphere (5% H<sub>2</sub>/Ar) during 5 h. This procedure guarantees an O/U ratio  
93 of 2.00 ± 0.01 and a high bulk density (97.5% of the theoretical density). The average grain size is  
94 11 μm, which is comparable to that of the LWR nuclear fuel. Pellets were polished on one side by the  
95 PRIMEVerre society (Montpellier, France) with diamond paste and then annealed twice. To degas  
96 adsorbed particles on the surface, samples were first annealed in a PECKLY© tubular furnace at 1000°C  
97 during 10 h under vacuum (10<sup>-7</sup> mbar). Then, a second annealing, at 1600°C for 4 h in a NABERTHERM©  
98 tubular furnace was performed under a 5%H<sub>2</sub>/Ar gas mixture flowing through ultra-high capacity  
99 oxygen and moisture filters. These conditions allow to anneal defects induced by the polishing and to  
100 maintain the UO<sub>2.00</sub> stoichiometry.

101 Next, pellets were implanted under vacuum ( $P < 5.10^{-6}$  mbar) with 800 keV <sup>133</sup>Cs<sup>2+</sup> ions at a fluence of  
102 10<sup>15</sup> Cs cm<sup>-2</sup>. A cooling device was used to maintain the sample temperature at 15°C in order to prevent  
103 any oxidation.

104 The Cs distribution and the displacements per atom (dpa) as a function of the implantation depth were  
105 computed using the SRIM software [14]. Threshold displacements values of U and O atoms were put  
106 at 40 eV and 20 eV respectively [15] and the code was run using the full cascade mode. Figure 1 shows  
107 a Cs profile corresponding to an implantation fluence of 10<sup>15</sup> at cm<sup>-2</sup>. It shows a quasi-Gaussian  
108 distribution centred at a mean projected range (Rp) of 140 nm with a maximum Cs concentration of  
109 0.08 at.%. The maximum number of 9 dpa at a depth of 80 nm indicates a high damage level in the

110 material. This value is only indicative as the SRIM code does not account for the material annealing  
111 occurring even at room temperature after each displacement cascade. As shown in a previous  
112 experimental work using Transmission Electron Microscopy (TEM) [16], these implantation conditions  
113 lead to the formation of two damaged regions. The first one, between the surface and about 85 nm  
114 from it, contains mainly point defects whereas the second one, that extends down to around 200 nm,  
115 shows mainly irradiation-induced dislocation loops.



116  
117 **Figure 1-** SRIM calculations of Cs concentration profile and number of dpa with respect to depth for a Cs  
118 implantation energy of 800 keV and a fluence of  $10^{15}$  Cs  $\text{cm}^{-2}$ .

119  
120 After implantation, pellets were annealed at different temperatures between 1000°C and 1600°C in a  
121 5% H<sub>2</sub>/Ar atmosphere to promote Cs migration in stoichiometric UO<sub>2</sub>. Cs depth profiles were measured  
122 by SIMS before and after annealing on a CAMECA IMS 7f facility equipped with an eucentric rotating  
123 sample stage designed by CAMECA to inhibit the surface roughening of poly-crystalline materials. Its  
124 velocity was set to 8 rpm for each analysis. A primary beam of 10 keV O<sub>2</sub><sup>+</sup> ions was used to sputter the  
125 UO<sub>2</sub> sample surface creating 250 × 250 μm<sup>2</sup> rasters. Secondary ions (<sup>238</sup>U<sup>16</sup>O<sup>+</sup> and <sup>133</sup>Cs<sup>+</sup>) were collected  
126 on the raster central part (62 μm diameter) to avoid wall effects. At least three craters were made for  
127 each SIMS analysis and three depth profiles (later averaged) were consequently obtained. More details  
128 about the experimental procedure and the data processing based on the relative sensitivity factor (RSF)  
129 can be found in [16].

130 Microstructural observations were also done at the JRC (Joint Research Centre) Karlsruhe, Germany.  
131 First, a FEI™ VERSA 3D Focused Ion Beam (FIB), was used to prepare electron transparent lamellae  
132 from the UO<sub>2</sub> samples. Samples were covered with a sputtered 40-50 nm gold layer and then a double  
133 platinum layer was deposited in the FIB, using the electron beam first and the ion beam then, to protect  
134 the surface during milling operations. Once the Pt deposit was made, two trenches were cut with the  
135 Ga<sup>+</sup> ion beam, then the remaining lamella was cut free from the sample, removed with an Omniprobe

136 needle and attached to a Cu grid. Thinning and final cleaning of the lamella were then performed at  
 137 decreasing voltages, taking extreme care not to consume the protecting layer and to avoid introducing  
 138 artefacts in the sample. The final thickness of the lamella varied between 30-60 nm. TEM analysis were  
 139 then performed with a 200 keV electron beam on a Tecnai G2 TEM FEI microscope. Both Bright Field  
 140 (BF) and High Resolution (HR) images were recorded at different sample areas, as well as energy  
 141 dispersive X-ray spectra.

142

## 143 2.2 Simulation method

### 144 2.2.1 Interatomic potentials and simulation parameters

145 Molecular statics (MS) and dynamics as well as NEB simulations were performed using the rigid ion (RI)  
 146 model (cf. equation 1) parameterised by Grimes and Catlow to study the stability of several FPs in UO<sub>2</sub>  
 147 [11]. To our knowledge, this is the only potential available in literature that includes cesium  
 148 interactions with oxygen and uranium. In this model, pair interactions are calculated using long-range  
 149 Coulombic interactions ( $q_i$  and  $q_j$  are the charges of the two ions) and a short-range Buckingham term.  
 150 A cut-off radius of 10.4 Å was set for all short-range interactions as done in [17]. Long-range Coulombic  
 151 interactions were computed using the Ewald summation [18]. All potential parameters are provided in  
 152 Table 1.

$$153 \quad V_{ij}(r_{ij}) = \frac{q_i q_j}{4\pi\epsilon_0 r} + A_{ij} e^{-\frac{r}{\rho_{ij}}} - \frac{C_{ij}}{r^6} \quad (\text{equation 1})$$

154

155 **Table 1-** Grimes and Catlow parametrization for UO<sub>2</sub> and Cs interatomic potentials [11].

	<b>U<sup>4+</sup>-U<sup>4+</sup></b>	<b>U<sup>4+</sup>-O<sup>2-</sup></b>	<b>O<sup>2-</sup>-O<sup>2-</sup></b>	<b>Cs<sup>+</sup>-U<sup>4+</sup></b>	<b>Cs<sup>+</sup>-O<sup>2-</sup></b>
<b>A<sub>ij</sub> (eV)</b>	18600	2494.20	108.00	18659.60	649.60
<b>ρ<sub>ij</sub> (Å)</b>	0.27468	0.34123	0.38000	0.29505	0.41421
<b>C<sub>ij</sub> (eV Å<sup>-6</sup>)</b>	32.64	40.16	56.06	48.62	64.34

156

157 Additional static simulations were performed using the core-shell (CS) model provided by Grimes and  
 158 Catlow [11] that allows for polarizability effects. In this model, each atom is modelled by a core linked  
 159 to its electronic shell by a harmonic spring, the net charge of the atom being computed as the sum of  
 160 both contributions (core and shell). In this case, the short-range interactions are computed from shell  
 161 interactions only. All the parameters used for the CS model can be found in [11]. The LAMMPS [19]  
 162 code is used for both the RI and CS models.

163

164

165

## 166 **2.2.2 Static calculations of intrinsic defect formation energy in UO<sub>2</sub>**

167 The formation energy of neutral intrinsic defects in UO<sub>2</sub>, i.e. Frenkel pairs and Schottky defects, were  
168 calculated using classical energy minimization of the system with and without the defect. Simulations  
169 were done using a 5 x 5 x 5 fluorite unit supercell (1500 atoms) and tri-periodic boundary conditions  
170 (PBC). This system size is large enough to constrain the influence of the replica while keeping  
171 reasonable cpu costs (see [17] for more details). Minimizations were achieved with the conjugate  
172 gradient algorithm using a force norm of 10<sup>-10</sup> eV.Å<sup>-1</sup> as a stopping criterion.

173 Using LAMMPS, the Frenkel pair formation energies were determined by calculating the energy  
174 difference between the defective lattice and the perfect one. For the Schottky defect, the formation  
175 energy relies on the cohesive energy of a UO<sub>2</sub> molecule to account for the number of atom variation.  
176 In addition to LAMMPS simulations, we used the Mott-Littleton approach implemented in GULP [20]  
177 to compare our results with those of Govers *et al.* [17]. The spheres radii within the Mott-Littleton  
178 approach were set to 9 and 20 Å respectively in accordance with [17].

179

## 180 **2.2.3 NEB calculations of Cs and U migration**

181 The Climbing Image (CI-) NEB method [21] is used to compute diffusion minimum energy paths (MEPs)  
182 of U and Cs atoms along the <100> and <110> directions in UO<sub>2</sub>. The system contains 1500 atoms and  
183 the simulations are performed using PBCs. The initial NEB path is made out of 17 interpolated replicas  
184 and is relaxed using the FIRE 2.0 damped dynamics minimizer [22,23] and a timestep of 0.1 ps. We  
185 chose the parallel nudging force to be based on interpolated ideal position and the perpendicular  
186 nudging force was computed to improve calculation convergence. The values of the parallel and  
187 perpendicular nudging forces between the replicas were both set to 5.0 eV Å<sup>-1</sup>. The stopping criterion  
188 of the simulation was set to a force tolerance of 0.01 eV Å<sup>-1</sup>.

189

## 190 **2.2.4 MD simulation of Cs diffusion in UO<sub>2</sub>**

191 The simulation temperature was fixed at 2227°C to improve Cs mobility statistics while being in the  
192 temperature range used in the literature experiments [5]. All MD simulations were performed using a  
193 timestep of 1 fs. First, the system is heated to the target temperature using a rate of 100°C/ps before  
194 being equilibrated for 50 ps in the NPT ensemble. Nosé-Hoover thermostat and barostat are used with  
195 relaxation times of 0.1 ps and 5.0 ps, respectively.

196 After equilibration, the mean square displacements (MSD) of each element (Cs, U, O) was computed  
197 in the NVE ensemble for a total time (N<sub>t</sub>) of 200 ps using equation 2.

$$198 \quad \langle \Delta r(t)^2 \rangle = \frac{1}{NN_t} \sum_{i=1}^N \sum_{t=t_0}^{N_t} (r_i(t + t_0) - r_i(t_0))^2 \quad (\text{equation 2})$$



199 Where:  $r_i(t)$  is the position of the  $i^{\text{th}}$  atom at time  $t$  ( $t_0$  being the beginning of the simulation),  $N$  is the  
200 total number of considered atoms and  $N_t$  is the MSD calculation total time.

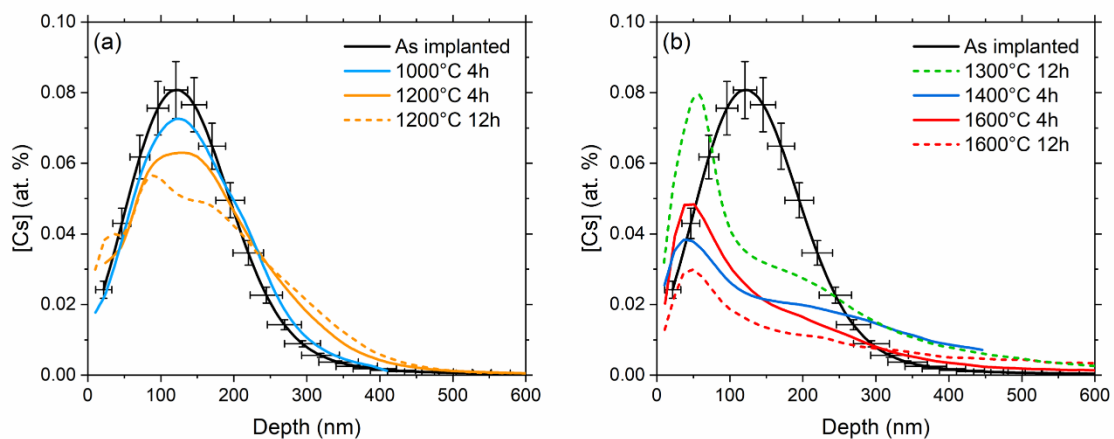
201  
202  
203

### 204 3. RESULTS

#### 205 3.1 Cesium thermal migration in $\text{UO}_2$ : experimental results

206 Figure 2 shows the cesium concentration distributions obtained by SIMS in  $\text{UO}_2$  samples implanted at  
207 a fluence of  $10^{15}$  Cs  $\text{cm}^{-2}$  after annealing between 1000 and 1600°C. They have been determined from  
208 the average roughness of SIMS craters (horizontal error bars) and from the RSF uncertainty (vertical  
209 error bars).

210



211

212 **Figure 2-** Cs depth profiles in  $\text{UO}_2$  samples implanted at  $10^{15}$  Cs  $\text{cm}^{-2}$  annealed under reducing atmosphere  
213 between 1000 and 1200°C (a) and between 1300 and 1600°C (b). The as-implanted sample's profile is the  
214 reference. Continuous lines are for 4h annealing and dashed ones for 12h annealing. Error bars have been  
215 added only on the as-implanted profiles in order to distinguish all depth profiles.

216

217 Figure 2(a) shows no significant Cs diffusion (nor release) in  $\text{UO}_2$  annealed at 1000°C (within the error  
218 bars). In contrast, profiles after annealing at 1200°C are significantly different even if no release was  
219 measured. Indeed, after four hours of annealing, the tail of the distribution (beyond 250 nm) is larger  
220 and the maximum concentration is lower. After twelve hours, the evolution of the Cs distribution is  
221 noteworthy as three maxima appear at around 30, 90 and 170 nm. This indicates the beginning of Cs  
222 migration processes (diffusion, trapping, ...) that change with depth, Cs local concentration and defect  
223 local concentration. The profile evolution initially observed at 1200°C seems to stabilize for  
224 temperatures larger than 1300°C where the depth profiles exhibit the same three peaks shape (see

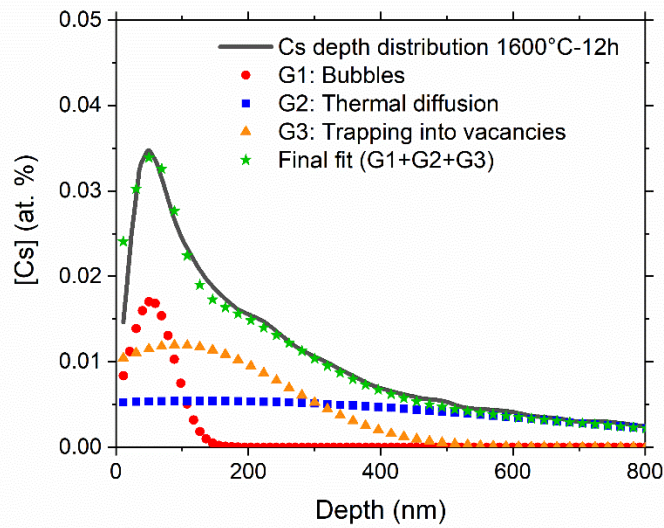
225 Figure 2(b)) but centred at different depths. At 1200°C, there is a first Cs peak at 50 nm from the  
226 surface, followed by a shoulder around 100 nm and a contribution at depths superior to 400 nm  
227 (beyond the end of the as-implanted profile), corresponding to Cs thermal diffusion. We note that no  
228 apparent release occurred at 1300°C (within the error bars). However, starting from 1400°C, significant  
229 release can be calculated: 40%, 35% and 48% for the 1400°C-4h, 1600°C-4h and 1600°C-12h annealing  
230 respectively<sup>1</sup>. To sum up, the non-steady state Cs diffusion occurs with the same mechanisms between  
231 1300°C and 1600°C but differs at 1200°C that is rather characterized by a transient regime. Therefore,  
232 no diffusion coefficient was determined at 1200°C in this study.

233 In order to determine the Cs diffusion coefficients in UO<sub>2</sub> at 1300, 1400 and 1600°C, each depth profile  
234 was first fitted using Gaussian curves. An example of a fit achieved on the Cs depth distribution  
235 measured after the 1600°C-12h annealing is presented in Figure 3. The fit with G1, G2 and G3 (Gaussian  
236 contributions) was done enforcing a maximum deviation of 5 nm for the maximum position of each  
237 Gaussian curve (respectively 50 nm from the surface, 140 nm and 100 nm), therefore restricting the  
238 total number of solutions to a few ones very close to each other.

239 The physical meaning of each contribution can be extrapolated from the work of Hocking *et al.* who  
240 used SIMS to profile iodine in polycrystalline UO<sub>2</sub> samples implanted with <sup>127</sup>I at 900 keV at a fluence  
241 of 10<sup>13</sup> at cm<sup>-2</sup> [24]. After annealing (between 1200 and 1650°C), Hocking *et al.* observed little evolution  
242 of the profile part corresponding to iodine concentrations above 10<sup>16</sup> at cm<sup>-3</sup> (~0.1 at.ppm). This was  
243 explained by iodine trapping in irradiation induced defects. Below this concentration threshold, in the  
244 tail of the profiles, iodine thermal (atomic) diffusion was highlighted. In our work, the G1 curve  
245 represents the Cs atoms trapped into faceted and spherical bubbles (see e.g., [16]) at 50 nm from the  
246 surface. The second Gaussian distribution (G3) accounts for the Cs atoms trapped into the vacancies  
247 created during implantation at around 100 nm, near the maximum of dpa calculated by SRIM (see  
248 Figure 1). There is also a possibility that these Cs atoms are trapped into nanobubbles not visible by  
249 microscopy with a size inferior to 1 nm. The third contribution (G2) is attributed to Cs thermal diffusion,  
250 since it was detected up to a depth of 800 nm in a zone free from implantation defects. We have  
251 chosen to centre it at a depth corresponding to the Rp (140 nm) of the as-implanted depth profile.  
252 Hence, this last contribution (G2) was used to determine the Cs diffusion coefficients.

---

<sup>1</sup> The 1400°C-4h distribution does not take into account the totality of the Cs in the sample as the SIMS analysis was stopped too early, thus leading to a probable overestimation of the Cs release from this sample but without changing the distribution shape and its straggling.



253

254 **Figure 3-** Fit of the Cs depth profile obtained after annealing at 1600°C-12h. The three Gaussian curves (G1, G2  
 255 and G3) represent Cs bubble formation, thermal diffusion and trapping into vacancies, respectively. The sum of  
 256 the three contributions fits the experimental curve.

257

258 Apparent diffusion coefficients  $D$  were determined using the Fick's second law as one of its analytical  
 259 solution is a Gaussian curve with standard deviation (noted  $\sigma_f$  or  $\sigma_i$ ) proportional to  $\sqrt{2Dt}$ . Considering  
 260 that both the initial (as-implanted) and final state of the Cs (annealed sample) are fitted with Gaussian  
 261 curves, we can thus deduce Cs diffusion coefficient using equation 3.

262 
$$D (cm^2 s^{-1}) = \frac{\sigma_f^2 - \sigma_i^2}{2t} \quad (\text{equation 3})$$

263 Values are reported in Table 2. Errors were determined from the uncertainty on the standard deviation  
 264 of the G2 curve and were calculated with the lowest and highest standard deviation values obtained  
 265 from each fit.

266

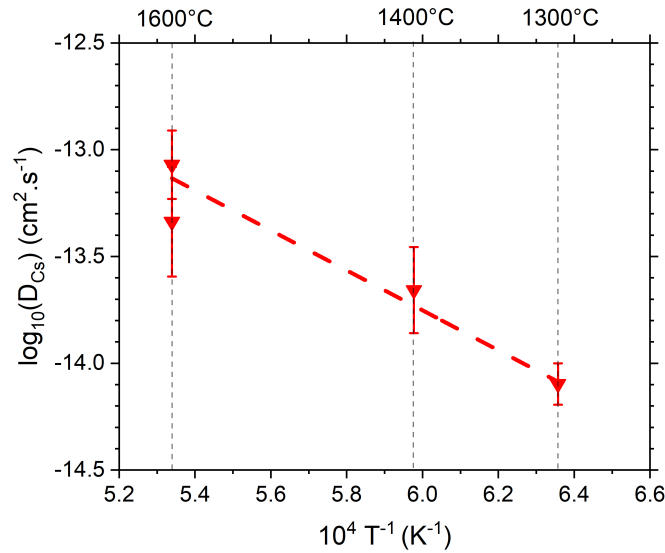
267 **Table 2-** Cs apparent diffusion coefficients and release fraction in UO<sub>2</sub> at 1300, 1400 and 1600°C. \*The Cs release  
 268 fraction is overestimated due to the fact that the concentration profile was not measured up to the end.

Annealing conditions	$D_{Cs}$ ( $10^{-14} \text{ cm}^2 \text{ s}^{-1}$ )	Cs release fraction
1300°C-12h	$0.8 \pm 0.2$	0 %
1400°C-4h	$2.2 \pm 1.3$	40 %*
1600°C-4h	$8.5 \pm 3.8$	35 %
1600°C-12h	$4.6 \pm 3.7$	48 %

269

270

271 The temperature dependence of Cs diffusion in  $\text{UO}_2$  is retrieved from the Arrhenius diagram presented  
272 in Figure 4 using a linear fit. Results lead to an activation energy of  $1.8 \pm 0.2$  eV and a pre-exponential  
273 factor equal to  $(8.4 \pm 5.6) \times 10^{-9} \text{ cm}^2 \text{ s}^{-1}$  for the Cs diffusion in  $\text{UO}_2$ .



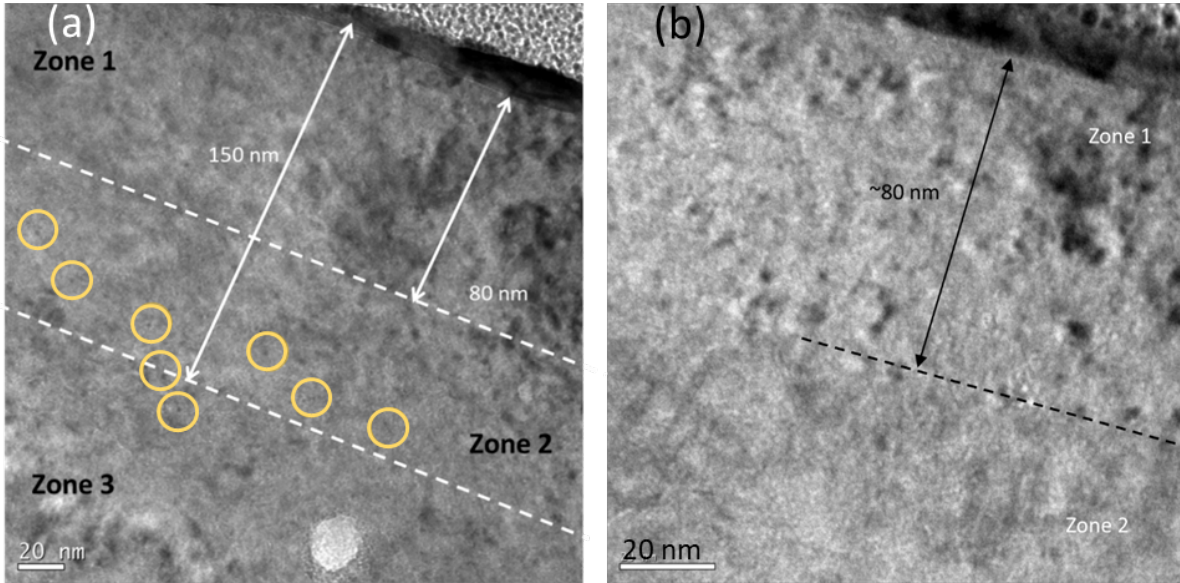
274

275 **Figure 4-** Arrhenius plot showing the temperature dependence of Cs diffusion coefficients in  $\text{UO}_2$

276

### 277 **3.2 Microstructure of the $\text{UO}_2$ sample annealed at 1200°C-12h**

278 The Cs profiles determined from the samples annealed at 1200°C (4h and 12h) display a transition  
279 between the profile of the sample annealed at 1000°C (no variation with respect to the as implanted  
280 sample) and the profiles of the samples annealed at 1300°C, 1400°C and 1600°C (which all exhibit a  
281 similar trend). Therefore, it was of particular interest to perform TEM analysis on the sample annealed  
282 at 1200°C – 12h. Figure 5 displays three zones which can be delimited at ~80 nm and ~150 nm from  
283 the surface. Zone 3 corresponds to the region free (or almost free) of implantation defects and some  
284 features (circled in yellow) can be seen near the zone 2 / zone 3 interface. The zone 1 / zone 2 interface  
285 corresponds to the maximum of the dpa profile as calculated by SRIM (see Figure 1).



286

287

288

289

290

291

292

293

294

295

296

297

298

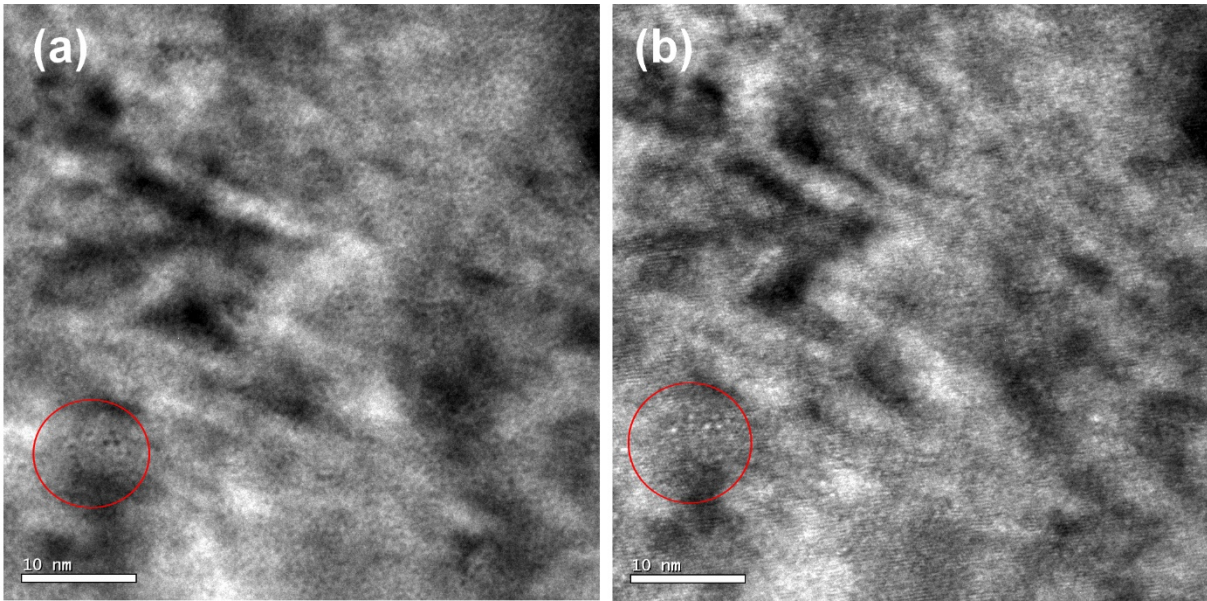
299

300

301

**Figure 5-** TEM image of the UO<sub>2</sub> sample implanted with cesium and annealed at 1200°C-12h. (a) illustration of the three different zones. (b) zoom at the zone 1 / zone 2 frontier. Yellow circles highlight features attributed to large bubbles.

At higher magnification, small features within zone 1 become visible. These features can be highlighted by acquiring over focused and under focused images of the same region, as shown in Figure 6. It can be seen that the contrast of each feature is inverted (from black to white or vice versa) when passing through focus, unlike what happens for strain contours. This clearly indicates presence of nanobubbles. Their exact size is not measurable due to the defocus, but it is certainly below 1 nm in agreement with what was recently observed by Onofri *et al.* [25]. Density values for the nanobubbles would be very difficult to calculate, due to their extremely small size as well as to the masking effect of the strain contours. Nevertheless, a very rough estimate based on the counting of visible bubbles in Figure 6, and considering an average thickness of 30 nm (based on the visibility of lattice fringes) would lead to a bubble density of the order of magnitude of  $10^{24}$  bubbles  $m^{-3}$ .

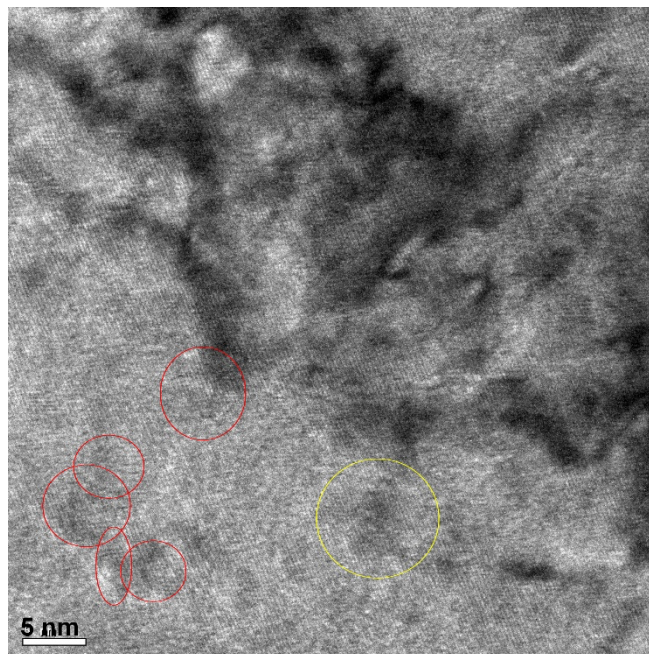


302  
303  
304  
305

**Figure 6-** TEM image of the UO<sub>2</sub> sample implanted with cesium and annealed at 1200°C-12h in zone 1 in under-focus (a) and over-focus (b) conditions. Red circle highlights the presence of several nanobubbles

306  
307  
308  
309  
310  
311

In zone 2 and zone 3, these nanobubbles are also present. Moreover, some bigger bubbles can be observed especially at a depth of around 160 nm from the surface (interface zone 2 / zone 3) where most of dislocations are present. The presence of dislocation segments is in agreement with what was found by He *et al.* on Kr-implanted UO<sub>2</sub> for similar damage levels [26]. Figure 7 presents a TEM image at the zone 2 / zone 3 interface showing such larger (~5 nm) bubbles. Some rare faceted bubbles around 5 nm in size can be also observed in Figure 7 (yellow circle).



312  
313  
314

**Figure 7-** HREM image at a depth of 160 nm from the surface of an UO<sub>2</sub> sample implanted with cesium and annealed at 1200°C-12h. In red, nanobubbles and in yellow, faceted bubble

315

316 The smaller, spherical nanobubbles, ~1 nm in size, can be observed until a depth of around 300 nm  
317 from the surface. These results are to be compared with those obtained at 1600°C in a previous study  
318 [16] where no bubbles were observed apart in a restricted area near the surface. They confirm that  
319 1200°C seems to be a threshold temperature in the migration of cesium in UO<sub>2</sub>.

320

321

### 322 3.3 Simulation results

#### 323 3.3.1 UO<sub>2</sub> intrinsic defect formation energies at 0K

324 UO<sub>2</sub> intrinsic defect formation energies (DFE) are presented in Table 3 where they are compared to  
325 DFT [27,28] and additional MS calculations performed by Sattonnay and Tetot [29] using the variable  
326 charge SMTB-Q interatomic potential. Two kind of defects were created: Frenkel Pairs (one vacancy  
327 and one interstitial far from each other) of oxygen or uranium and Schottky defects (one uranium  
328 vacancy and two oxygen vacancies).

329

330 **Table 3-** DFE (eV) of intrinsic neutral defects in UO<sub>2</sub> calculated with Grimes potential with the rigid ion (RI) model  
331 and the core shell (CS) model, using LAMMPS and GULP codes. FP = Frenkel Pairs. S = Schottky defects. Three  
332 possible configurations exist to place the oxygen vacancies around the uranium vacancy in the <100> (S1), <110>  
333 (S2) or <111> (S3) direction.

Model	This work			CS model <i>GULP</i> [17]	SMTB-Q [29]	DFT [27,28]
	RI model <i>LAMMPS</i>	CS model <i>LAMMPS</i>	CS model <i>GULP</i>			
<b>FP<sub>O</sub></b>	7.8	7.0	5.8	5.8	4.4	5.3
<b>FP<sub>U</sub></b>	28.2	24.8	18.9	18.9	6.1	15.8
<b>S1</b>	8.9	8.1	7.3	7.3	5.9	10.7
<b>S2</b>	9.2	8.4	7.0	7.0	5.9	
<b>S3</b>	10.5	9.5	7.2	7.2	6.4	

334

335 Overall values obtained using the RI or the CS models are in good agreement with both DFT and SMTB-  
336 Q literature results. Our values obtained for the CS model using GULP (identical to those already  
337 published [17]) are higher than the ones found by DFT except for the value of the Schottky defect. For  
338 DFT calculations, the Schottky defect corresponds to three vacancies without interaction (explaining  
339 the sole configuration in the table) which leads to a high energy of 10.7 eV. It can be noted that the  
340 SMTB-Q value of the FP<sub>U</sub> DFE is much lower than the value found with other potentials. This can be  
341 explained by the fact that no U-U interaction is implemented in the SMTB-Q formalism. As pointed out  
342 by Grimes [30], empirical potentials can be comparable to those predicted by quantum mechanical  
343 procedures but suffer from two main factors: (i) the equilibrium interatomic spacings, and (ii) the way

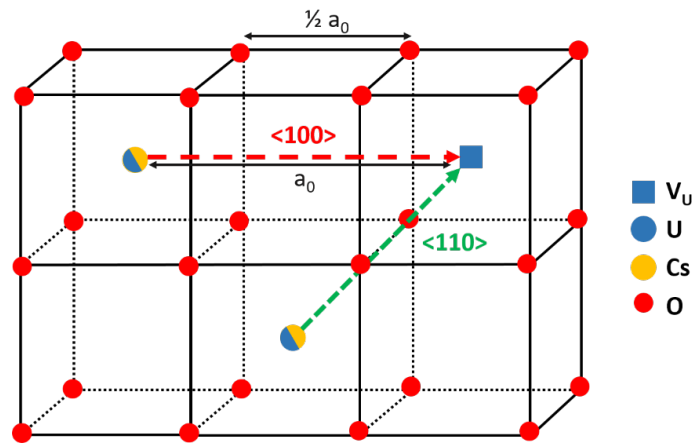
344 electronic polarisation is handled. This explains the discrepancies even if the use of the Mott-Littleton  
 345 method is supposed to correct these factors. The DFE values calculated with LAMMPS (without the  
 346 Mott-Littleton method) are higher. Nevertheless, the order of magnitude is respected when compared  
 347 to DFT: the FP<sub>0</sub> DFE is the more stable while the FPU has a higher energy. In the following, we chose  
 348 to use the Grimes RI model to investigate Cs migration processes from a qualitative point of view due  
 349 to its acceptable accuracy and in order to save a lot of computation time.

350

### 351 3.3.2 Cs and U migration energies in UO<sub>2</sub> at 0K using NEB simulations

352 The migration of Cs and U atoms in UO<sub>2</sub> were computed using the CI-NEB method for several sets of  
 353 configurations including various point defects.

354 Uranium dioxide has the fluorite crystalline structure with a lattice parameter equal to 5.47 Å. The  
 355 fluorite structure is made of a face-centred cubic U sublattice surrounding a simple cubic O sublattice  
 356 which has a periodicity of  $a_0/2$ . Migration paths of Cs within the fluorite structure are schematized in  
 357 Figure 8.



358

359 **Figure 8-** Migration paths of cesium (yellow) or uranium (blue) along the <100> (red arrow) and <110>  
 360 directions (green arrow), towards a uranium vacancy (blue square) in the UO<sub>2</sub> oxygen sub-lattice (red circles).

361

362 Table 4 shows the activation energies computed for the migration of a U or Cs atom initially located  
 363 into a uranium vacancy and migrating along the <100> or <110> direction as described in Figure 8 (red  
 364 and green arrows). Results are compared to DFT based literature data [9]. U or Cs atom migration to a  
 365 uranium vacancy is more favourable along the <110> direction than along the <100> one. While  
 366 migration energies obtained using the Grimes potentials are, in most cases, slightly overestimated,  
 367 they remain in qualitative agreement with DFT results except for the Cs migration along the <100>  
 368 direction. It is found to be less favourable than the U migration in the <110> direction in contradiction  
 369 with DFT predictions.

370



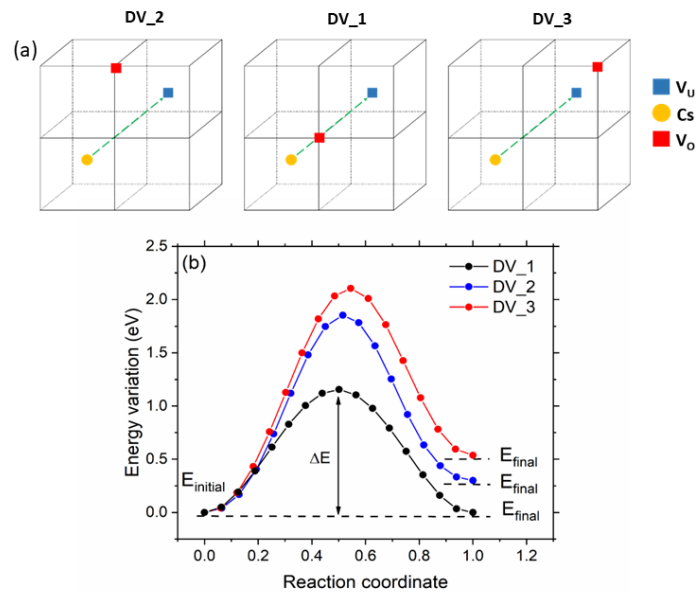
371  
 372  
 373  
 374

**Table 4-** Migration energies (eV) of Cs and U through a vacancy mechanism along directions  $\langle 100 \rangle$  and  $\langle 110 \rangle$  in  $\text{UO}_2$

<i>Direction of migration</i>	U		Cs	
	$\langle 100 \rangle$	$\langle 110 \rangle$	$\langle 100 \rangle$	$\langle 110 \rangle$
<b>This work (CI-NEB) with the Grimes potential [11]</b>	14.8	7.95	10.53	1.67
<b>DFT (NEB) from [9]</b>	8.24	5.60	4.6	2.7

375  
 376

377 CI-NEB calculations were also performed in systems containing a Cs atom and a divacancy (DV) which  
 378 is a defect composed of one uranium vacancy and one oxygen vacancy. Eight configurations are  
 379 possible to place the oxygen vacancy in one of the summits of the cube hosting the uranium vacancy.  
 380 However, according to symmetries, only three DV configurations (DV\_1, DV\_2 and DV\_3) are unique  
 381 as illustrated in Figure 9(a). Figure 9(b) presents the energy variation as a function of the normalised  
 382 distance between the initial and final states for the three configurations.



383  
 384  
 385  
 386  
 387  
 388

**Figure 9-** Migration of Cs towards divacancies (DV) (a) Schematic representation of the DV\_1, DV\_2 and DV\_3 configurations in which Cs migration energies were calculated along the  $\langle 110 \rangle$  direction. For more clarity, only the vacancies and the Cs atom are depicted in the oxygen sub-lattice (black lines). (b) Energy variation of the system as a function of the normalized distance between the NEB initial and final states.

389 Figure 9(b) displays a symmetric energy landscape for the DV\_1 configuration with an activation energy  
 390  $\Delta E$  equal to 1.15 eV. For the other configurations DV\_2 and DV\_3, the final energy of the system is

391 higher than the initial one resulting in a backward migration energy lower than in the forward case.  
392 Activation energies are presented in Table 5.

393

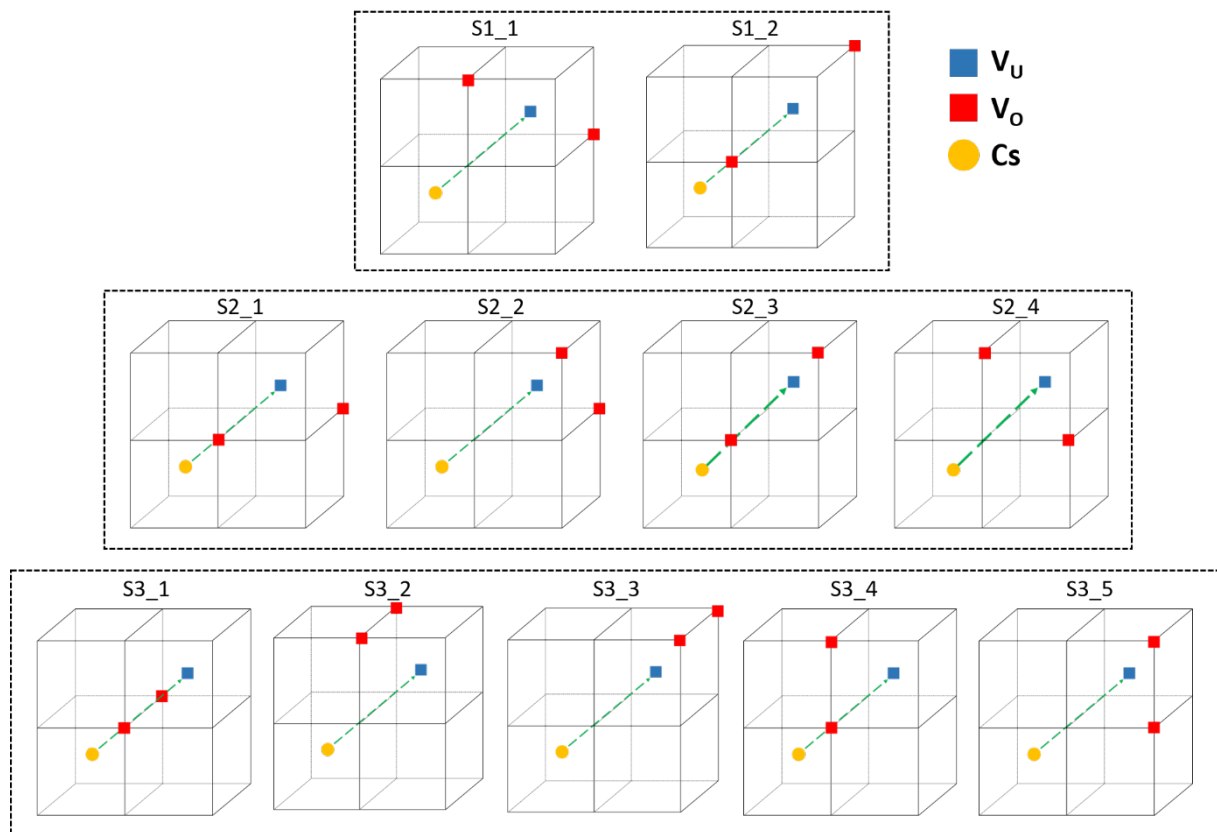
394 **Table 5-** Backward and forward migration energy of Cs along the direction  $\langle 110 \rangle$  towards divacancies (DV)

		DV_1	DV_2	DV_3
395				
396	$\Delta E$ (eV)	1.15	1.55	1.57
397		1.15	1.85	2.11
398	<i>Number of equivalent configurations</i>	2	4	2
399				

400 These results emphasize the influence of the oxygen vacancy location on the Cs migration energy.  
401 Indeed, the migration barrier decreases as the oxygen vacancy get closer to the Cs atom at the saddle  
402 point. The lower activation energy ( $\Delta E = 1.15$  eV) corresponds to the closest position of  $V_o$ , obtained  
403 for the DV\_1 configuration. For the two other configurations, DV\_2 and DV\_3, as the  $V_o$  gets further,  
404 the calculated energy increases up to 1.55 eV and 2.11 eV, respectively.

405

406 Finally, we determined the migration energies of a Cs atom originally located in a uranium vacancy  
407 going toward each non-equivalent configuration of a Schottky defect (S1, S2 or S3). Eleven unique  
408 Schottky configurations were determined with S3\_1 being the only symmetric configuration. They are  
409 depicted in Figure 10 and the corresponding activation energies are gathered in Table 6.



411

412 **Figure 10-** Schematic representation of the eleven different Schottky configuration considered to calculate Cs413 migration energies, along the  $\langle 110 \rangle$  direction, in the uranium vacancy of a Schottky defects. For more clarity,

414 only the vacancies and the Cs atom are depicted in the oxygen sub-lattice (black lines).

415

416

417

418 **Table 6-** Forward and backward migration energies of Cs along the direction  $\langle 110 \rangle$  within different Schottky419 defect configurations in  $\text{UO}_2$ 

420

		S1		S2				S3				
		S1_1	S1_2	S2_1	S2_2	S2_3	S2_4	S3_1	S3_2	S3_3	S3_4	S3_5
$\Delta E$ (eV)	Backward	1.54	0.74	0.87	1.28	0.78	1.60	0.48	1.43	1.19	1.10	-
	Forward	2.20	1.33	1.26	2.15	1.37	2.23	0.49	2.16	2.34	1.50	-
<i>Number of equivalent config.</i>		2	2	4	4	2	2	1	2	1	2	4

421

422 The results presented in Table 6 can be grouped within three families. The first one corresponds to

423 configurations where the Cs atom has to go through the oxygen lattice to reach the uranium vacancy.

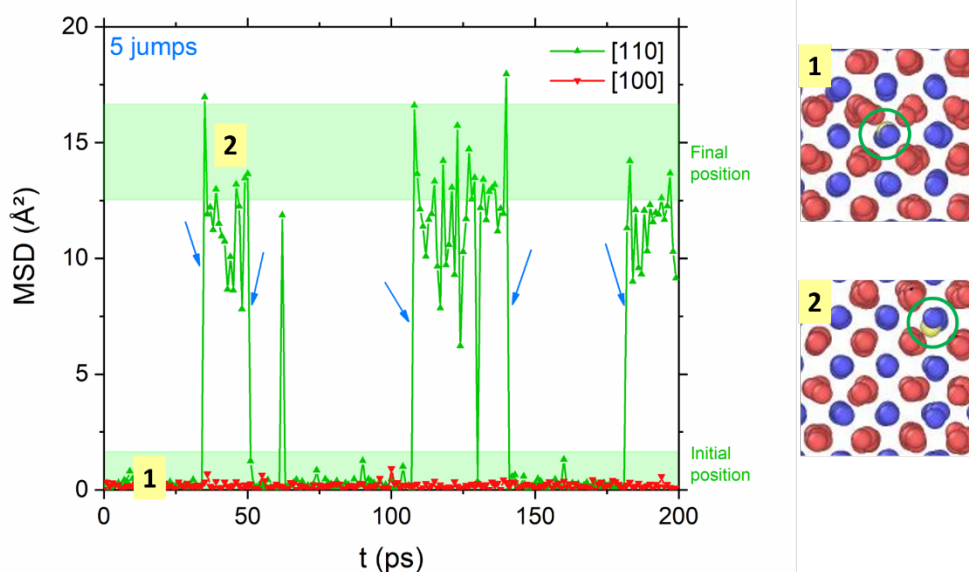
424 In this case, the Cs forward migration energy ranges between 2.15 and 2.36 eV. The second family  
 425 concerns an oxygen vacancy between the Cs atom and the uranium vacancy, at a distance of  $\frac{a_0}{2}\sqrt{3}$ .  
 426 For these configurations, the Cs forward migration energy is comprised between 1.26 and 1.50 eV.  
 427 Finally, when both oxygen vacancies are close to the Cs atom (S3\_1), the migration barrier is very low,  
 428 with a value of 0.49 eV. We were not able to determine the Cs barrier migration of the S3\_5  
 429 configuration due to the unwanted migration of one of the  $V_o$ , resulting in the formation of a S2\_3  
 430 Schottky.

431

### 432 3.3.3 MD simulation of Cs migration at high-temperature

433 The same initial configurations than for the NEB calculations were chosen to run MD simulations at a  
 434 temperature of 2227°C. During the runs, each atom was free to move according to local forces and  
 435 thermal fluctuations. However, despite the elevated temperature, uranium atoms and  $V_U$  created for  
 436 each configuration were shown to remain immobile. This behaviour is attributed to the activation  
 437 energy ( $> 7.95$  eV as shown in Table 4) which is really high precluding U self-diffusion to happen in our  
 438 simulation times.

439 As a first step, we computed the Cs MSD as a function of time for a Cs atom incorporated into a VU  
 440 close to another VU along the direction  $\langle 110 \rangle$  or along the  $\langle 100 \rangle$  one. In total, 11 runs were performed  
 441 for each direction to obtain statistically meaningful results. An example is displayed in Figure 11(a). We  
 442 observe that the value of the Cs MSD oscillates between the Cs initial position (MSD = 0 Å<sup>2</sup>) and the  
 443 position inside the uranium vacancy (MSD value of  $\sim 15$  Å<sup>2</sup>). This confirms that a Cs atom jumps  
 444 between the two uranium vacancies which are displayed on the right side of the Figure 11. From this  
 445 specific simulation, we counted five Cs jumps indicated by blue arrows in Figure 11.

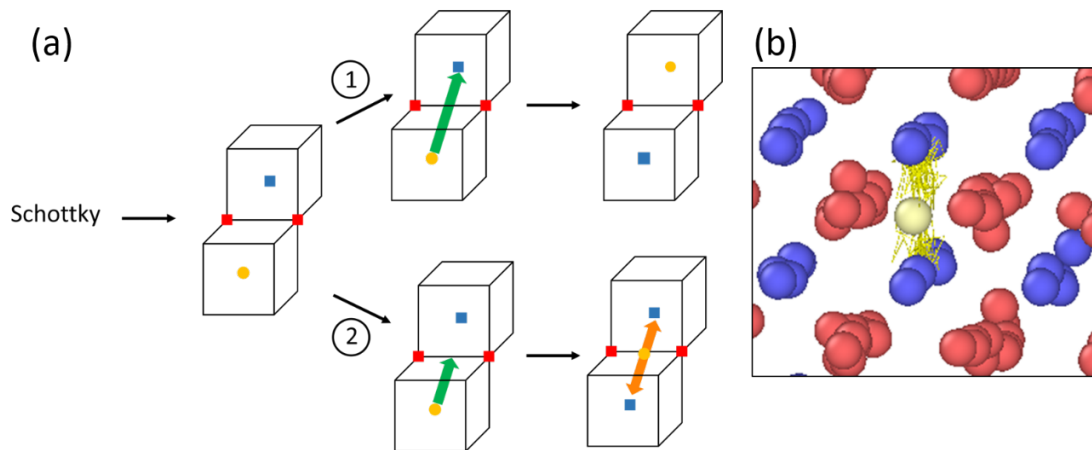


446

447 **Figure 11-** Example of a MSD evolution of Cs with time for a temperature of 2227°C. Initially, the Cs atom is  
448 placed in a  $V_U$  and can diffuse in another  $V_U$  along the  $\langle 110 \rangle$  or the  $\langle 100 \rangle$  direction (positions 1 and 2 shown on  
449 the right side). The arrows indicate the jumps of Cs in the uranium vacancy. To help the interpretation, green  
450 bands indicate the MSD values corresponding to the Cs initial position ( $MSD = 0 \text{ \AA}^2$ ) and the final position (in  
451  $V_U$ ) of the Cs atom for  $\langle 110 \rangle$  direction, centred around the theoretical MSD value of  $\sim 15 \text{ \AA}^2$  (the square of the  
452 distance between the Cs atom and the  $V_U$  which is  $\frac{a_0\sqrt{2}}{2}$ )

453  
454 No Cs diffusion along the  $\langle 100 \rangle$  direction (red curve in Figure 11) was recorded which can be explained  
455 by the high corresponding energy barrier of 10.5 eV. On the contrary, an average performed on the  
456 whole eleven simulations shows  $4.7 \pm 3.0$  Cs jumps along the  $\langle 110 \rangle$  direction. This indicates that, even  
457 if Cs atoms are mobile in  $UO_2$ , the Cs diffusion is impeded by the even lower self-diffusion of U as  
458 already discussed in [9,10]. In this case, the frame-by-frame analysis of the simulations allowed us to  
459 highlight an indirect mechanism for the Cs diffusion. The intermediate state corresponds to a Cs  
460 position between two oxygen atoms, at mid-distance of the two  $V_U$  (see Figure 8). This corresponds to  
461 the saddle point identified in the corresponding CI-NEB calculation. The MD simulations show two  
462 cases when the Cs atom approaches closer to this saddle point. The first one corresponds to a failed  
463 attempt, which results in a sharp peak between a MSD value decreasing from  $\sim 15 \text{ \AA}^2$  down to  $\sim 7.5 \text{ \AA}^2$   
464 (Figure 11). In this case, the Cs atom goes back to its departure site. The second one relates to a  
465 successful attempt, which matches with a MSD value changing from  $\sim 15 \text{ \AA}^2$  down to  $\sim 0 \text{ \AA}^2$ . In all our  
466 simulations, the Cs atom jump from  $V_U$  to another  $V_U$  implies the formation of an oxygen vacancy  
467 created from one of the two oxygen atoms located near the saddle point. The oxygen atom « kicked  
468 out » in an interstitial position can move afterwards in the lattice.

469 Cesium MSD was also computed in systems containing either a divacancy or a Schottky defect.  
470 Calculations were made for the three divacancy configurations (DV\_1, DV\_2 and DV\_3) and also for  
471 the S1, S2 and S3 Schottky configurations. In our simulation conditions, oxygen vacancies become  
472 mobile around 1527°C. Thereby, as the temperature increases during the simulations, we  
473 systematically observed a rearrangement of the oxygen atoms in the DV and the Schottky defects that  
474 resulted in the symmetric configurations DV\_1 and S3\_1, respectively, that are the most favourable  
475 defects as previously calculated by CI-NEB. Averaging the number of Cs atomic jumps in 200 ps, for  
476 each DV simulations, leads to  $4.7 \pm 3.1$  jumps. This value is quasi identical to the result obtained for  
477 the sole uranium vacancy configuration. This is explained by the fact that when the Cs atom goes  
478 through the saddle point, the configuration remains the same. An oxygen vacancy must be created to  
479 allow the Cs jump.



480  
481  
482  
483  
484  
485  
486

**Figure 12-** (a) Illustration of the two possible cases (namely (1) and (2) on the figure) for the Cs behavior after S3\_1 formation with temperature, the Cs atom either jumps easily in the uranium vacancy or is stabilized at the center of the tetravacancy thus formed. Caption is identical to previous figures. (b) OVITO visualization of the trajectory (yellow line) of an atom of Cs (yellow) stabilized in a tetravacancy, jumping continuously between the two uranium vacancies.

487 For the Schottky simulations, we observed two cases. In half of the runs, the Cs atom was stabilized in  
488 the centre of the tetravacancy created by the Cs atom leaving its initial site. Then, an endless back and  
489 forth movement of the Cs atom in each uranium vacancy occurs (Figure 12 (b)). For the other half  
490 simulations, we obtained an average of  $11.2 \pm 1.8$  jumps which agrees with the energy barrier value,  
491 the lowest of all those calculated using the CI-NEB methods.

492  
493  
494  
495

#### 496 4. DISCUSSION

497 It is quite well-known that Cs forms bubbles at low temperature. At a temperature threshold of 600°C,  
498 Sabathier *et al.* [31] highlighted the formation of 1.7 nm sized Cs bubbles in UO<sub>2</sub> implanted with cesium  
499 at a fluence of 10<sup>16</sup> at cm<sup>-2</sup>. Moreover, bubbles of around 1-2 nm were observed in UO<sub>2</sub> implanted with  
500 cesium at a fluence of 10<sup>15</sup> at cm<sup>-2</sup> after a 1000°C annealing [16]. As long as the trapping into bubble  
501 prevails, no Cs long range diffusion can occur. This is why below 1200°C, the cesium distribution is  
502 unchanged compared to the as-implanted one in our study. Therefore, between 600°C and 1000°C,  
503 cesium migration at short range can only occur to allow Cs bubble nucleation into defects like those  
504 created by implantation. The nucleation centre of these small bubbles is most probably a defect  
505 containing at least a uranium vacancy since Cs incorporation energies into a single uranium vacancy, a  
506 divacancy and a Schottky defect are negative according to DFT calculations [9].

507 At 1200°C, only slight changes appear in the Cs distribution after four hours annealing. However, a  
508 remarkable evolution was observed after twelve hours with the apparition of three peaks. TEM  
509 observations were performed on this latter sample. Nanobubbles of around 1 nm in size were observed  
510 within the first 300 nm from the surface which corresponds to the presence of the implanted cesium  
511 atoms. Three regions were delimited. The first Zone corresponds roughly to the two first peaks  
512 observed by SIMS. A very rough density estimate was calculated for zone 1, yielding an order of  
513 magnitude of  $10^{24}$  nanobubbles  $m^{-3}$ . A similar estimate could not be performed in the other zones.  
514 However, it can be qualitatively estimated that the  $\sim 1$  nm sized nanobubble density is higher at the  
515 bottom of zone 1 ( $\sim 60$ - $80$  nm from the surface) than in proximity of the surface. In zone 2 and zone 3,  
516 we could observe some bigger bubbles ( $\sim 5$  nm) and some rare faceted bubble of the same size. This  
517 means that some coalescence process has occurred at the place where a maximum of defects and Cs  
518 concentration can be found. These few bubbles show that 1200°C is really a threshold temperature to  
519 start the migration of cesium which can lead to the growth of some bubbles and the disappearance of  
520 smaller bubbles as it was observed at 1600°C in [16]. However, since the Cs peaks position observed  
521 in the SIMS profiles evolves with the annealing time, no diffusion coefficient was calculated at 1200°C.  
522 Nevertheless, these peaks may be the premises of the three contributions distinguished in the Cs  
523 distributions obtained in the 1300-1600°C temperature range. Two of them are explained by the  
524 trapping of cesium atoms into implantation defects and the last one is attributed to Cs diffusion  
525 occurring after thermal resolution process. They were respectively fitted by Gaussian distributions  
526 named G1, G3 and G2. G1 distribution accounts for cesium atoms trapped into bubbles near the  
527 surface (at  $\sim 50$  nm) where most of point defects are created by the implantation process. These  
528 bubbles have grown from spherical to bigger faceted bubbles through an Ostwald mechanism as  
529 explained in ref. [16]. Faceted bubbles growth is certainly favoured by the surface proximity: the flux  
530 of vacancies brought by the surface at high temperature may form clusters of defects able to stabilize  
531 these bubbles. This is consistent with Murphy *et al.* [32] MD simulations, which have shown that xenon  
532 was particularly stable in nanovoids formed by several Schottky defects. However, the growth of these  
533 faceted bubbles seems to be limited. At 1300°C, no Cs release was observed, which means that Cs  
534 diffusion towards the surface (in the long range) is not effective due to the trapping of Cs into bubbles  
535 at  $\sim 50$  nm from the surface. On the contrary, important releases were observed at 1400°C and 1600°C  
536 (35 to 50%) and the accumulation peak was significantly lower. Thus, as the temperature increases,  
537 the equilibrium between long-range diffusion and trapping mechanisms changes: above 1300°C, the  
538 diffusion process is favoured over the trapping, when maximum size and/or density of faceted bubbles  
539 is reached. G3 distribution is also attributed to a trapping of cesium atoms into implantation induced  
540 defects. At depths greater than 50 nm, TEM analysis did not show any Cs bubble [16]. As the Cs  
541 solubility limit in UO<sub>2</sub> (around  $\sim 0.01$  at.% at 1700°C according to [33]) is exceeded in this second

542 distribution, this would suggest a competition between thermal resolution process, diffusion and  
 543 trapping of the Cs atoms. Our MD simulations show that at high temperature, the Cs atoms can easily  
 544 jump from a uranium vacancy to another type of defect containing a uranium vacancy, with the  
 545 exception of the tetravacancy. Since there are no vacancy sources available nearby as opposed to the  
 546 trapping contribution of G1, no bigger defects can form to stabilize the Cs bubbles. We thus  
 547 hypothesise that only small clusters of cesium and vacancies are created limiting thereafter the Cs  
 548 diffusion. Finally, the G2 distribution corresponds to Cs diffusion towards the bulk material, in a region  
 549 where the Cs concentration is around the solubility limit. This region is free from point defects but  
 550 contains some dislocation loops created by the implantation collision cascades [16]. To further  
 551 understand the effect of defects on the Cs migration in UO<sub>2</sub>, some activation energies found in the  
 552 literature for different conditions of irradiation and temperature are reported in Table 7.

553  
554

555 **Table 7-** Comparison of the pre-exponential factors ( $D_0$ ) and activation energies ( $E_a$ ) of Cs diffusion in UO<sub>2</sub> fuel  
 556 available in the literature compared to our value (bold)

Sample history	T (°C)	$D_0$ (cm <sup>2</sup> s <sup>-1</sup> )	$E_a$ (eV)	Ref.
Post-irradiation annealing BU: 47 GW.d.t <sub>U</sub> <sup>-1</sup>	1500 - 2500	2.1 10 <sup>-8</sup>	1.6	[34]
<b>UO<sub>2</sub> implanted with at 10<sup>15</sup> at cm<sup>-2</sup> and annealed</b>	<b>1300 - 1600</b>	<b>5.6 10<sup>-9</sup></b>	<b>1.8</b>	<b>This work</b>
Post-irradiation annealing 38 < BU < 44 GW.d.t <sub>U</sub> <sup>-1</sup>	1200 - 2200	7.6 10 <sup>-3</sup>	3.2	[35]
Post-irradiation annealing 10 < BU < 30 GW.d.t <sub>U</sub> <sup>-1</sup>	1200 - 2200	2.0 10 <sup>-3</sup>	4.2	[35]
Post-irradiation annealing Slightly irradiated UO <sub>2</sub> (~1 ppb of Cs)	1450 - 1750	3.4 10 <sup>-2</sup>	4.3	[8]

557

558 Table 7 displays a wide range of activation energies values, from 1.6 eV to 4.3 eV, which implies  
 559 different Cs migration mechanisms (assuming no deviation of the stoichiometry). First, we will consider  
 560 the experiment of Prussin et al. with only 1 ppb of cesium in a very slightly irradiated UO<sub>2</sub> sample [8].  
 561 Almost no irradiation induced defects are produced. The formation of uranium vacancies is only  
 562 activated by the temperature (between 1450 and 1750°C) during each annealing. Therefore, only a  
 563 small fraction of vacancies is available for Cs diffusion and the uranium diffusion is the limiting process.  
 564 This corresponds to our MD simulations where no jumping of uranium atoms occurred, preventing Cs  
 565 from diffusing, despite its ability to jump between uranium vacancies. The activation energy calculated  
 566 by DFT for the diffusion of a uranium atom towards an uranium vacancy is 5.6 eV [9]. This value is  
 567 close, even if slightly higher, to the one found by Prussin *et al.* (4.3 eV) [8] and the one found by

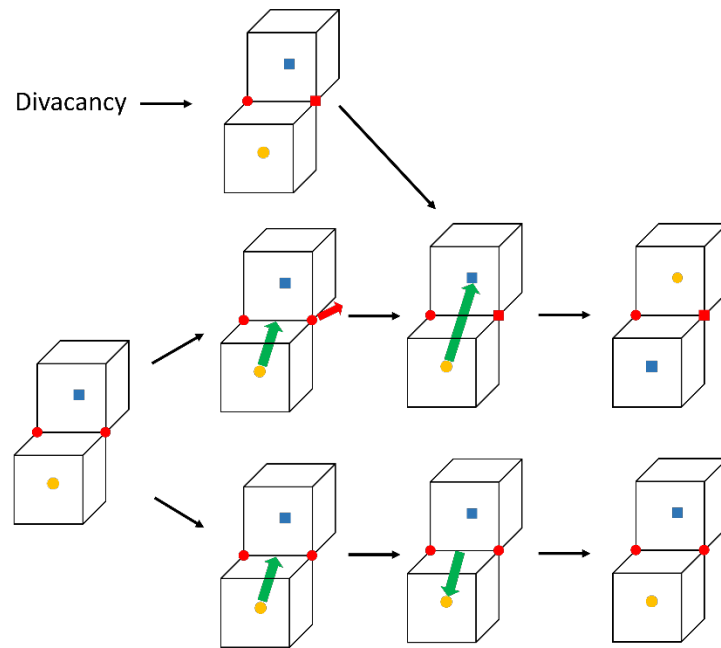


568 Osborne *et al.* (4.2 eV) [35] for irradiation experiments done at low burnup (maximum value of  
569 30 GW.d.tU<sup>-1</sup>).

570 On the contrary, Kudo *et al.* [34] measured a low activation energy of 1.6 eV in a highly damaged UO<sub>2</sub>  
571 sample indicating that uranium diffusion is no more the limiting step for the Cs diffusion because of  
572 the presence of a high concentration of defects. Similarly, we obtained a low value (1.8 eV) because of  
573 the annealing of extended defects created during the implantation process, thus creating a flux of point  
574 defects, especially vacancies enhancing the Cs diffusion.

575 Besides, our MD simulations outline the role of oxygen atoms on Cs diffusion in UO<sub>2</sub>, which can be  
576 considered as a Cs diffusion mechanism assisted by oxygen vacancies. Indeed, MSD calculations always  
577 resulted in an oxygen migration enhanced by the presence of the cesium atom, independently of the  
578 initial configuration. Considering the particular case of the Schottky defect, regardless of the initial  
579 Schottky type, it invariably results in the symmetric configuration (S3\_1) where the two oxygen  
580 vacancies are between the Cs atom and the V<sub>U</sub>. If the Cs atom (initially in V<sub>U</sub>) migrates at the centre of  
581 the defect, it forms a tetravacancy, where it can be stabilised. However, CI-NEB calculation in this  
582 configuration resulted in a particularly low value for Cs internal migration (~0.5 eV). Thus, if we  
583 consider formation of others vacancies close to the tetravacancy, this could lead to an enhanced  
584 diffusion process. Then, the Cs atomic diffusion would only rely on oxygen vacancy diffusion between  
585 the different uranium vacancies.

586 Concerning divacancies, they behave similarly to the Schottky defects, ending up each time in the  
587 symmetric configurations (DV\_1). For initial configurations where there is only one V<sub>U</sub> in the system,  
588 an oxygen vacancy is created by oxygen migration following the Cs atom attempts to jump as  
589 illustrated in Figure 13. Hence, the most probable migration path for the Cs atom seems to be through  
590 a sole oxygen vacancy. The corresponding barrier migration energy calculated by CI-NEB is around  
591 1.2 eV, which is of the same order of magnitude than in our experiment. Of course, the Grimes  
592 interatomic potentials have been found to underestimate the Cs diffusion into V<sub>U</sub> in comparison with  
593 the DFT value. However, this mechanism with the oxygen vacancy should have a lower activation  
594 energy in DFT than the one with only the uranium vacancy which would be closer to the values found  
595 by the different experiments.



596

597 **Figure 13-** Illustration of the Cs migration assisted by one oxygen vacancy between two uranium vacancies in  
 598 direction  $\langle 110 \rangle$ . For initial configuration without a  $V_O$  initially present, the Cs jump requires that an oxygen atom  
 599 leave, otherwise the attempt to reach the  $V_U$  fail. Caption is identical to previous figures

600

601 Finally, to be able to observe (by MD simulations) Cs diffusion through the  $UO_2$  crystal, several uranium  
 602 vacancies should be initially placed in the system to allow the Cs atom to diffuse through this  
 603 predefined path. Such calculations are not advised, as they would generate too many additional  
 604 charges in a system that is rather small (1500 atoms) in the first place. Another solution would be to  
 605 develop Cs interactions with U and O with a potential such as the SMTB-Q potential that is already  
 606 available to efficiently describe U and O interactions in an effective manner [27,36,37].

607

608

## 609 5. CONCLUSION

610 The aim of this paper was to investigate the Cs migration in  $UO_2$  to obtain a better understanding of  
 611 its behaviour in the fuel, especially under accidental conditions at high temperature. SIMS experiments  
 612 highlighted the complex behaviour of cesium between  $1000^\circ\text{C}$  and  $1600^\circ\text{C}$ . This behaviour is the  
 613 consequence of the competition between several mechanisms, each one prevailing at different  
 614 temperatures. At relatively "low" temperatures up to  $1000^\circ\text{C}$ , Cs mainly forms nanometric bubbles  
 615 which results in no apparent diffusion within the timescale of the laboratory.  $1200^\circ\text{C}$  seems to be a  
 616 threshold temperature at which the motion of the cesium atoms and the subsequent untrapping  
 617 process occur. This mainly indicates a thermal resolution mechanism which allows Cs atoms to migrate  
 618 at short distances. Between  $1300^\circ\text{C}$  and  $1600^\circ\text{C}$ , Cs bubbles exist only in a very limited zone near the

619 surface. Elsewhere, thermal resolution prevails allowing Cs atoms to diffuse. We established a model  
620 to estimate apparent Cs diffusion coefficients from the depth profiles and we determined an activation  
621 energy of 1.8 eV which is one of the smallest compared to the literature data. The atomistic simulations  
622 show that this low value is due to the Cs atoms jumping towards defects containing a uranium vacancy  
623 without being limited by the uranium diffusion. This is the case in our experiments, where high  
624 concentration of vacancies is created by the annealing of the extended defects (mainly interstitial  
625 dislocation loops) formed during the implantation process. The combination of CI-NEB and MD  
626 simulations show that the most probable process to explain Cs atomic diffusion is through a U-O  
627 divacancy. Two configurations were identified at the saddle point. If an oxygen vacancy exists, the  
628 cesium atom can go through it freely. Otherwise, an oxygen vacancy is always created before allowing  
629 the Cs migration.

630

631

## 632 **Acknowledgements**

633 The authors thank Anthony Duranti (IP2I Lyon, France) for the Cs implantation at the IMIO400  
634 implanter, Dr. Philippe Sainsot for interferometry measurements (INSA Lyon, France) and M. Mommey  
635 and Y. Giraud (IP2I Lyon, France) for their help with the HPC.

636

## 637 **AIP Publishing data sharing policy**

638 The data that support the findings of this study are available from the corresponding author upon  
639 reasonable request.

## 640 **References**

- 641 [1] D. Champion, I. Korsakissok, D. Didier, A. Mathieu, D. Quélo, J. Groell, E. Quentric, M.  
642 Tombette, J.P. Benoit, O. Saunier, V. Parache, M. Simon-Cornu, M.A. Gonze, P. Renaud, B. Cessac, E.  
643 Navarro, A.C. Servant-Perrier, Radioprotection 48, 11 (2013). doi:10.1051/radiopro/2012052.
- 644 [2] G. Ducros, P.P. Malgouyres, M. Kissane, D. Boulaud, M. Durin, Nucl. Eng. Des. 208, 191 (2001).  
645 doi:10.1016/S0029-5493(01)00376-4.
- 646 [3] Y. Pontillon, G. Ducros, Nucl. Eng. Des. 240, 1867 (2010).  
647 doi:10.1016/j.nucengdes.2009.06.028.
- 648 [4] A. Hidaka, T. Kudo, T. Nakamura, H. Uetsuka, J. Nucl. Sci. Technol. 39, 273 (2002).  
649 doi:10.1080/18811248.2002.9715185.
- 650 [5] T. Kudo, M. Kida, T. Nakamura, F. Nagase, T. Fuketa, J. Nucl. Sci. Technol. 44, 1421 (2007).  
651 doi:10.1080/18811248.2007.9711389.
- 652 [6] Y. Pontillon, E. Geiger, C. Le Gall, S. Bernard, A. Gallais-During, P.P. Malgouyres, E. Hanus, G.  
653 Ducros, J. Nucl. Mater. 495, 363 (2017). doi:10.1016/j.jnucmat.2017.08.021.
- 654 [7] A.H. Booth, A method of calculating fission gas diffusion from UO<sub>2</sub> fuel and its application to  
655 the X-2-f loop test, 1957.
- 656 [8] S.G. Prussin, D.R. Olander, W.K. Lau, L. Hansson, J. Nucl. Mater. 154, 25 (1988).  
657 doi:10.1016/0022-3115(88)90115-8.
- 658 [9] F. Gupta, A. Pasturel, G. Brillant, J. Nucl. Mater. 385, 368 (2009).  
659 doi:10.1016/j.jnucmat.2008.12.009.
- 660 [10] G. Busker, R.W. Grimes, M.R. Bradford, J. Nucl. Mater. 279, 46 (2000). doi:10.1016/S0022-  
661 3115(99)00274-3.
- 662 [11] R.W. Grimes, C.R.A. Catlow, Philos. Trans. R. Soc. London. Ser. A Phys. Eng. Sci. 335, 609 (1991).  
663 doi:10.1098/rsta.1991.0062.
- 664 [12] J.P. Crocombette, J. Nucl. Mater. 305, 29 (2002). doi:10.1016/S0022-3115(02)00907-8.
- 665 [13] G. Brillant, F. Gupta, A. Pasturel, J. Phys. Condens. Matter. 21, 285602 (2009).  
666 doi:10.1088/0953-8984/21/28/285602.
- 667 [14] J.F. Ziegler, U. Littmark, J.P. Biersack, Stopping and ranges of ions in matter, Pergamon Press,  
668 New York, 1985.
- 669 [15] J. Soullard, J. Nucl. Mater. 135, 190 (1985). doi:10.1016/0022-3115(85)90077-7.
- 670 [16] C. Panetier, Y. Pipon, C. Gaillard, N. Moncoffre, T. Wiss, D. Mangin, O. Dieste, B. Marchand, R.  
671 Ducher, R. Dubourg, T. Epicier, L. Raimbault, J. Nucl. Mater. 543, 152520 (2021).  
672 doi:10.1016/j.jnucmat.2020.152520.

673 [17] K. Govers, S. Lemehov, M. Hou, M. Verwerft, J. Nucl. Mater. 366, 161 (2007).  
674 doi:10.1016/j.jnucmat.2006.12.070.

675 [18] P.P. Ewald, Ann. Phys. 369, 253 (1921). doi:10.1002/andp.19213690304.

676 [19] S. Plimpton, Fast Parallel Algorithms for Short-Range Molecular Dynamics, J. Comput. Phys.  
677 117, 1 (1995).

678 [20] J.D. Gale, A.L. Rohl, Mol. Simul. 29, 291 (2003).

679 [21] G. Henkelman, B.P. Uberuaga, H. Jónsson, J. Chem. Phys. 113, 9901 (2000).  
680 doi:10.1063/1.1329672.

681 [22] E. Bitzek, P. Koskinen, F. Gähler, M. Moseler, P. Gumbsch, Phys. Rev. Lett. 97, 1 (2006).  
682 doi:10.1103/PhysRevLett.97.170201.

683 [23] J. Guérolé, W.G. Nöhring, A. Vaid, F. Houllé, Z. Xie, A. Prakash, E. Bitzek, Comput. Mater. Sci.  
684 175, 109584 (2020). doi:10.1016/j.commatsci.2020.109584.

685 [24] W.H. Hocking, R.A. Verrall, I.J. Muir, J. Nucl. Mater. 294, 45 (2001). doi:10.1016/S0022-  
686 3115(01)00447-0.

687 [25] C. Onofri, C. Sabathier, G. Carlot, D. Drouan, C. Bachelet, C. Baumier, M. Gérardin, M. Bricout,  
688 Nucl. Instrum. Meth. B 463, 76 (2020). doi: 10.1016/j.nimb.2019.11.031

689 [26] L-F. He, M. Gupta, C. A. Yablinsky, J. Gan, M. A. Kirk, X.-M. Bai, J. Pakarinen, T. R. Allen, J. Nucl.  
690 Mater. 443, 71 (2013). doi: 10.1016/j.jnucmat.2013.06.050

691 [27] B. Dorado, D.A. Andersson, C.R. Stanek, M. Bertolus, B.P. Uberuaga, G. Martin, M. Freyss, P.  
692 Garcia, Phys. Rev. B - Condens. Matter Mater. Phys. 86, 1 (2012). doi:10.1103/PhysRevB.86.035110.

693 [28] B. Dorado, M. Freyss, B. Amadon, M. Bertolus, G. Jomard, P. Garcia, J. Phys. Condens. Matter.  
694 25, 333201 (2013). doi:10.1088/0953-8984/25/33/333201.

695 [29] G. Sattonnay, R. Tétot, Bulk, J. Phys. Condens. Matter. 25, 125403 (2013). doi:10.1088/0953-  
696 8984/25/12/125403.

697 [30] R.W. Grimes, C.R.A. Catlow, A.M. Stoneham, J. Phys. Condens. Matter. 1, 7367 (1989).  
698 doi:10.1088/0953-8984/1/40/011.

699 [31] C. Sabathier, L. Vincent, P. Garcia, F. Garrido, G. Carlot, L. Thome, P. Martin, C. Valot, Nucl.  
700 Instrum. Meth. B 266, 3027 (2008). doi:10.1016/j.nimb.2008.03.158.

701 [32] S.T. Murphy, A. Chartier, L. Van Brutzel, J.P. Crocombette, Phys. Rev. B - Condens. Matter  
702 Mater. Phys. 85, 1 (2012). doi:10.1103/PhysRevB.85.144102.

703 [33] C.T. Walker, C. Bagger, M. Mogensen, J. Nucl. Mater. 240, 32 (1996). doi:10.1016/S0022-  
704 3115(96)00477-1.

705 [34] T. Kudo, M. Kida, T. Nakamura, F. Nagase, T. Fuketa, J. Nucl. Sci. Technol. 44, 1428 (2007).  
706 doi:10.3327/jnst.44.1428.

- 707 [35] M. Osborne, R.A. Lorenz, ORNL studies of fission product release under LWR severe accident  
708 conditions, Nucl. Saf. 33 (1992).
- 709 [36] D. MBongo, R. Tetot, R. Ducher, R. Dubourg, N. Salles, J. Phys. Condens. Matter. 32, 095701  
710 (2019).
- 711 [37] A. Soulié, E. Clouet, F. Garrido, J.-P. Crocombette, A. Kraych, G. Sattonnay, Acta Mater. 150,  
712 248 (2018). doi:10.1016/j.actamat.2018.03.024.